



## **Performance prediction for interacting wing sails: A viscosity-corrected non-linear lifting line model compared to wind tunnel experiments at pre-**

Downloaded from: <https://research.chalmers.se>, 2026-04-17 06:02 UTC

Citation for the original published paper (version of record):

Malmek, K., Larsson, L., Everyd Bensow, R. et al (2026). Performance prediction for interacting wing sails: A viscosity-corrected non-linear lifting line model compared to wind tunnel experiments at pre- and post-stall conditions. *Ocean Engineering*, 345. <http://dx.doi.org/10.1016/j.oceaneng.2025.123598>

N.B. When citing this work, cite the original published paper.



ELSEVIER

Contents lists available at ScienceDirect

## Ocean Engineering

journal homepage: [www.elsevier.com/locate/oceaneng](http://www.elsevier.com/locate/oceaneng)

## Research paper

# Performance prediction for interacting wing sails: A viscosity-corrected non-linear lifting line model compared to wind tunnel experiments at pre- and post-stall conditions

Karolina Malmek <sup>a,b,\*</sup>, Lars Larsson <sup>b</sup>, Rickard E. Bensow <sup>b</sup>, Christian Finnsgård <sup>a</sup>

<sup>a</sup> RISE Research Institutes of Sweden, The Safety and Transport division, Maritime Department, Gothenburg, 412 58, Sweden

<sup>b</sup> Department of Mechanics and Maritime Sciences, Chalmers University of Technology, Gothenburg, 412 96, Sweden

## ARTICLE INFO

## Keywords:

Non-linear lifting line method  
Performance prediction  
Wind propulsion  
Wind-assisted propulsion system (WAPS)  
Sail-sail interaction  
Wind tunnel experiments  
Wing sail

## ABSTRACT

As wind propulsion for ships emerges as a key measure to meet climate goals, there is an increasing need for effective performance prediction methods. This paper presents an efficient non-linear lifting line method (ISILL), enhanced with viscous corrections, specifically developed for interacting sails. The validation is conducted against wind tunnel experiments, covering a wide range of sheeting combinations, both pre- and post-stall conditions, at four different apparent wind angles. The results focus on predicting maximum driving force, corresponding sheeting angles, and yaw moment of the sail system. Up to and including the onset of stall, the overall agreement with wind tunnel experiments is satisfactory. The method remains computationally stable beyond the point of stall, although the accuracy decreases in the post-stall regime.

## 1. Introduction

Regulatory bodies have set increasingly strict targets for the reduction of greenhouse gases (GHGs) for long-distance shipping (IMO, 2023; Parliament, 2023). As a consequence, wind propulsion technologies (WPTs), such as rotor sails, wing sails, suction/active wings, kites and modern sailing rigs, have generated increasing attention as a measure of reducing fuel consumption and CO<sub>2</sub> emissions. Several WPTs have shown promising energy-saving potential and operational viability (Kolodziejcki and Sosnowski, 2025). For example, operational reports from ArianeGroup/OceanWings (OceanWings, 2024) indicate energy savings of 30%-50% using wing sails onboard the Canopée. In mid-2024, 45 ships around the world had adopted wind propulsion technologies (Veritas, 2024), with more than 100 installations by the end of the year (Kolodziejcki and Sosnowski, 2025).

To further adopt and optimize the use of wind propulsion technology, computational tools are needed to predict and compare fuel savings (Gerhardt et al., 2022). In 2024, the Specialist Committee on Wind Powered and Wind Assisted Ships of the 30th International Towing Tank Conference (ITTC) (Alterskjær et al., 2024) published the first guidelines and recommendations on how to predict power savings of wind-powered ships. Typically, predicting the power-saving potential includes the use of velocity prediction programs (VPPs). In the programs, several different subsystems need to be modeled; the WPT, the

hydrodynamic forces on hull and rudders, machinery and other propellers, such as a conventional propeller. VPPs need to be combined with accurate routing studies and weather forecasting. In addition to power prediction, VPPs form a base for voyage simulators, which can be used to evaluate operational safety and in crew training.

To model a WPT, the aerodynamic forces generated by the sails need to be estimated. Such simulations are not trivial, as for a system of multiple finite-aspect ratio sails, sail-sail interaction and 3D effects need to be considered. These types of complex fluid flows may be evaluated using high-fidelity methods, i. e., computational fluid dynamics (CFD) or experimental fluid mechanics (EFD). Different CFD methods have been applied to model interacting wing sails, such as, Reynolds-averaged Navier-Stokes (RANS) and improved delayed detached eddy simulation (IDDES) (Zhu et al., 2024; Xu et al., 2025). Due to the large variation in the possible headings of the ship in relation to the incoming wind (i.e. apparent wind angles) and the large number of possible sail sheeting combinations, the high computational cost of CFD limits its application in design optimization and in VPPs (Malmek et al., 2024). EFD can allow for evaluating a WPT at a range of angles of attack and apparent wind angles; however, at a high financial cost. In addition, scale effects and experimental uncertainties must be considered.

An alternative to high-fidelity methods are potential flow-based models, which are orders of magnitude more computationally efficient compared to RANS CFD codes. One such group of methods is based

\* Corresponding author.

E-mail address: [karolina.malmek@ri.se](mailto:karolina.malmek@ri.se) (K. Malmek).

## Nomenclature

$\beta_{AW}$	Apparent wind angle
CE	Centre of Effort
VPP	Velocity Prediction Program
$\alpha_i$	Angle of attack of Sail $i$
$C_L$	Lift coefficient (3D)
$C_D$	Drag coefficient (3D)
$V_\infty$	Freestream (apparent) wind speed
$\rho$	Air density
$S$	Sail area of a single sail
$n_{\text{sails}}$	Number of sails
$d$	Half the distance between Sail 1 and Sail 3
$x$	Direction of the driving force (ship forward axis)
$AR$	Aspect ratio of the sail
$c$	Average chord length of the sail
$s$	Sail height
$Re$	Reynolds number
$c_l$	Sectional lift coefficient (2D)
$c_d$	Sectional drag coefficient (2D)
$C_L^{2D}$	Integrated 2D lift coefficient (infinite span)
$C_D^{2D}$	Integrated 2D drag coefficient (infinite span)
$AR$	Aspect ratio of the sail
$\hat{y}_i$	Predicted value from the ISILL model
$y_i$	Observed value from wind tunnel experiments
$n$	Number of observations in statistical analysis
MAE	Mean Absolute Error
MSD	Mean Signed Deviation
$C_X$	Force coefficient in the $x$ -direction (driving force)
$C_M$	Yaw moment coefficient
$C_Y$	Side force coefficient
CFD	Computational Fluid Dynamics
EFD	Experimental Fluid Dynamics
WPT	Wind Propulsion Technology
NLL	Nonlinear Lifting Line
SILL	Sectionally Integrated Lifting Lines
ISILL	Interacting Sectionally Integrated Lifting Lines

on Prandtl's lifting-line theory, with modifications by, for example, Weissinger (1947). In order to include viscous effects, these classical theories are coupled with 2D empirical sectional data, and the resulting theory is commonly known as nonlinear lifting line (NLL) theory. Various adaptations of this theory exist within the aerospace industry and are used in the preliminary design stages (Gallay and Laurendeau, 2015; Beyer et al., 2024).

Modeling of sails using the NLL theory was suggested by Graf et al. (2014) and Dupont et al. (2019), basing their models predominantly on the work of Phillips and Snyder (2000) respectively (Anderson, 1991). Persson and Werner (2019) presented and validated a simplified version of the theory and applied it to a single wing sail, calling it sectionally integrated lifting lines (SILL). It applies a fixed elliptical lift distribution to estimate the 3D effects, thereby avoiding iterations. The SILL code has been shown to be robust and gives acceptable results up to the onset of stall for a single sail. Malmek et al. (2020, 2024) further developed the SILL method by including interaction effects between multiple sails.

The use of NLL codes within a wind propulsion context was further extended, for example, by Kramer and Steen (2022), applying the  $\Gamma$ -coupled iterative solver proposed by Anderson (1991). Recently, Schot and Garenaux (2023) and Babarit (2024) have presented adaptations of NLL models, showing promising results for both wing and rotor sails. In contrast to Malmek, the aforementioned authors suggest an iterative approach to estimate the 3D downwash effect on the sail itself, allowing for a more correct representation of the lift distribution over the sail. However, several challenges with these variants have been reported: 1) code instabilities when approaching the onset of stall requires extensive

relaxation (Phillips and Snyder, 2000; Gallay and Laurendeau, 2015) which increase computational time, 2) sensitivity to the number of segments used in the discretization of the lifting line (Schot and Garenaux, 2023), and 3) they have been shown to fail to capture the lift distribution in the post-stall regime, showing oscillatory behavior between discretizations segments (Gallay and Laurendeau, 2015; Schot and Garenaux, 2023). Updated solving algorithms, such as the one proposed by Gallay and Laurendeau (2015), and alternative approaches to updating the local angle of attack (Van Dam, 2002) may remedy these issues, but these variants of the NLL models have not yet been implemented and validated in the context of wind propulsion.

This study evaluates the Interacting Sectionally Integrated Lifting Lines (ISILL) method proposed by Malmek (2023). The sail-sail interaction is modeled iteratively using horseshoe vortices and the effect of downwash on each individual sail is modeled by the SILL method. By applying an assumed lift distribution, the calculation time is reduced and the stability of the code is increased compared to a NLL model with varying lift distribution. Viscous 2D data, based on CFD or wind tunnel tests, is used as pre-tabulated input to the model. Additionally, Malmek et al. (2024) suggests a viscous correction to compensate for boundary layer effects around the onset of stall, thereby improving the prediction of maximum potential thrust generated by the WPT.

In the present paper, wind tunnel experiments with three wing sails are used to validate the ISILL code. A large test matrix is presented, with pre- and post-stall systematic sheeting variations, at four different apparent wind angles. For post-stall angles, validation against EFD is preferred to RANS CFD, as RANS has limited accuracy for separated flows. This paper thus complements and extends previous validation studies of the ISILL code (Malmek et al., 2024).

Three new key questions are investigated in this paper:

- *Can the method be applied to predict the onset of stall?* Identifying the onset of stall is crucial when optimizing the WPT for maximum driving force. In addition, the method should correctly predict the corresponding sheeting angles and yaw moment.
- *What is the accuracy and method behavior post-stall?* The sails are assumed to mainly operate at pre-stall angles, but post-stall flow may occur in off-conditions. The code should remain stable for post-stall angles to accommodate integration in a VPP.
- *How to generate sectional input data, in practice?* A novel approach is applied by calibrating the 2D input data using single-sail 3D measurements. This approach is in line with practical application of the method, as 3D standalone lift and drag data, obtained either by measurements or simulations, are commonly given by technology providers.

The paper structure is as follows. The first part gives information about the test case and validation data, by presenting the geometry and test matrix in Section 2.1 and the wind tunnel experiments in Section 2.2. This is followed by a brief description of the ISILL method in Section 3. The two ways that viscous effects are introduced in the model are detailed in Section 3.1, describing the use of single-sail results to calibrate the model input, and in Section 3.2, describing a correction to compensate for interaction effects on boundary layer development. Section 4.1 gives information regarding how tunnel blockage effects are handled in the modeling. The validation results are presented in Section 4. Finally, the conclusions and suggestions for future investigations are given in Section 5.

## 2. Validation data

This section presents the geometry, the sheeting and apparent wind angle combinations used in the validation and data acquisition.

### 2.1. Geometry and definitions

The geometry used in the validation consists of three wing sails placed on a flat surface. The sail design is based on a concept used as

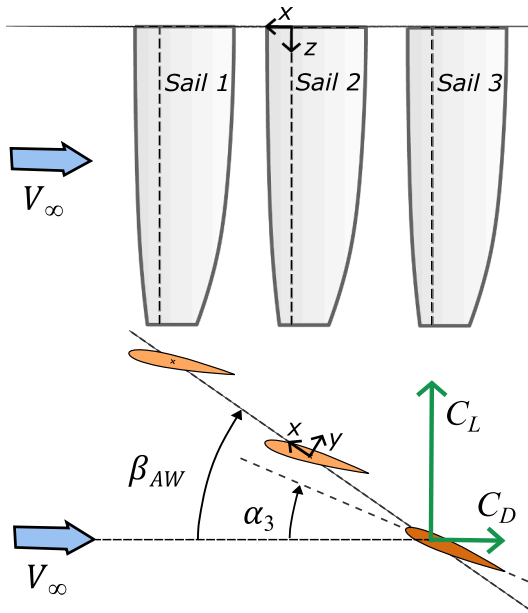


**Fig. 1.** Side view (top) and plan view (bottom) of the wing sails used in the test case. Blue arrows indicate freestream wind direction ( $V_\infty$ ). Since the model is stationary, the freestream wind corresponds to both true and apparent wind. The apparent wind angle ( $\beta_{AW}$ ), the angle of attack for Sail 3 ( $\alpha_3$ ), the lift coefficient ( $C_L$ ) and the drag coefficient ( $C_D$ ) are defined. The origin of the  $xyz$  coordinate system is at the quarter-chord of Sail 2.

**Table 1**  
Principal dimensions of the model used in wind tunnel tests.

Parameter	Symbol	Value
Number of sails	$n_{sails}$	3
Sail height	$s$	1385 mm
Average chord	$c$	400 mm
Maximum chord		460 mm
Sail area (single sail)	$S$	0.552 m <sup>2</sup>
Aspect ratio	$AR$	3.5
Mast to mast spacing	$d$	748 mm

a research test case in the Oceanbird (now Orcele) car-carrier project, and has been used in several related research projects (Werner et al., 2023; Dhomé, 2024). The model is 1:58 of the full-scale design and the model dimensions are presented in Table 1.

The section profile of the sails is a NACA0015 section and the plan-form can be seen in Fig. 1. The center of rotation is located at 25% of the chord length (quarter-chord). The apparent wind angle,  $\beta_{AW}$ , is defined relative to the WPT centerline, which is assumed to coincide with both the centerline and the heading of an (imaginary) ship it is placed upon. Consequently, the driving force generated by the WPT is here defined as the force generated in the direction of the  $x$ -axis in Fig. 1, and gives a measure of the total propulsive force generated by the sail system. The driving force is normalized by  $0.5\rho V_\infty^2 S n_{sails}$  to form the driving force coefficient,  $C_X$ . The side force coefficient,  $C_Y$  corresponds to the normalized force generated in the direction of the  $y$ -axis. The yaw moment coefficient,  $C_M$ , is defined by dividing the moment generated by Sail 1 and Sail 3 around the mast-foot of Sail 2 (i.e., the origin in Fig. 1) by  $2d$ ,

$$C_M = \frac{C_{Y,1}d - C_{Y,3}d}{2d}, \quad (1)$$

where  $2d$  is the distance between Sail 1 and Sail 3.

**Table 2**

Systematic sheeting variations for Sail 1 and Sail 3 in relation to Sail 2. For each series of variations, the angle of attack of Sail 2 was fixed at  $\alpha_2 = 0^\circ, 5^\circ, 10^\circ, 15^\circ, 17^\circ$  and  $19^\circ$ . All sheeting combinations were repeated for apparent wind angles  $\beta_{AW} = 15^\circ, 30^\circ, 60^\circ$  and  $90^\circ$ .

Sail 1	Sail 2	Sail 3
$-5^\circ$	$\alpha_2$	$+5^\circ$
$-2^\circ$	$\alpha_2$	$+2^\circ$
$-1^\circ$	$\alpha_2$	$+1^\circ$
$\pm 0^\circ$	$\alpha_2$	$\pm 0^\circ$
$+1^\circ$	$\alpha_2$	$-1^\circ$
$+5^\circ$	$\alpha_2$	$-5^\circ$
$-2^\circ$	$\alpha_2$	$+7^\circ$
$+2^\circ$	$\alpha_2$	$+2^\circ$

## 2.2. Wind tunnel experiments

The experiments were performed in the R.J. Mitchell wind tunnel at Southampton University, a closed-circuit wind tunnel with cross-section dimensions of 3.5 m  $\times$  2.4 m and a turbulence intensity level of less than 0.2% (Castro, 2021). The experimental campaign was part of the Oceanbird wind powered car carrier project and has been covered in several publications. The first presentation of the experimental setup and results was given by Giovannetti et al. (2022). Further experimental results were included in the licentiate thesis of Malmek (2023). Wielgosz et al. (2025) used the single-sail results to investigate scale effects and performed an uncertainty analysis. The experimental results were also used by Xu et al. (2025) to validate an improved delayed detached eddy simulation (IDDES) CFD setup to investigate the effects of multiple wing sail interaction.

The model, consisting of three sails, was mounted in a row hanging from the tunnel roof balance, as illustrated in Fig. 1. Different apparent wind angles relative to the ship sailing at different angles relative to the wind were achieved by rotating the roof balance. The overall forces were measured with a six-component Nuntem load cell balance. The individual forces and moments of each sail were also measured with separate transducers. Thin sheets of foam plastic were added to the tunnel roof to ensure that no gap between the bottom of the sails and the roof remained.

The freestream wind speed during all tests was set to 25 m/s. This corresponded to a Reynolds number of  $6.76 \times 10^5$ , based on the mean chord length, which is within the flow regime where laminar boundary layer effects may be substantial. To try to ensure transition to the turbulent flow regime, a zigzag transition tape was placed at the quarter-chord on both sides of each sail.

At higher angles of attack, mechanical load limits prevented rotating the sails at a constant speed of 25 m/s. Therefore, tests above angles of ca  $17^\circ$ – $19^\circ$  had to be performed by lowering the wind speed to 10 m/s before rotating the sails and, after setting the new sheeting angles, returning the speed to 25 m/s. The single-sail wind tunnel tests showed that this process of lowering the wind speed induced a hysteresis effect, where the sail stalled at lower angles of attack, as shown in Fig. 3.

While the previous publications of the experiments reported no blockage effect for the single sail, this study found a blockage effect for the multi-sail tests, which will be discussed further below.

The uncertainties in the wind tunnel tests for the single sail measurements, using the individual force transducer of Sail 2, have been evaluated by Wielgosz et al. (2025). The percentage uncertainty in  $C_L$  and  $C_D$  for pre-stall angles are approximately 4% respectively 35% of the measured value. Even though the drag force is generally much smaller than the lift force, the rather high uncertainty in  $C_D$  could give an effect when calculating the driving force at low apparent wind angles. When sailing upwind, the drag component has a larger impact on the driving force  $C_X$ . To investigate the impact of this uncertainty, the  $C_X$  values measured by summing the contributions of the individual

**Table 3**  
Angles of attack for Sail 1 and Sail 3 during sweeps of Sail 2 from  $\alpha_2 = -15^\circ$  to  $20^\circ$ .

$\beta_{AW}$	Sail 1	Sail 2	Sail 3
$30^\circ$	$13^\circ$	$\alpha_2$	$17^\circ$
$90^\circ$	$15^\circ$	$\alpha_2$	$15^\circ$

force transducers were compared with those predicted by the overhead balance. The maximum  $C_X$  value measured by the two different balances differed 0.2%, 1.5% and 0.9% for apparent wind angles  $30^\circ$ ,  $60^\circ$  and  $90^\circ$ . At the lowest apparent wind angle measured,  $\beta_{AW} = 15^\circ$ , the maximum  $C_X$  differed by 0.02, giving a percentage error of 13%.

The uncertainty analysis above did not include geometry errors, such as geometry deviations or misalignment of the sail angle. The sails were mounted using a frame to ensure alignment. When studying the single sail results, a small shift of the lift curve can be observed (it is not symmetric around  $\alpha = 0$ ). By interpolation between the results in the linear lift regime ( $-10^\circ$  to  $10^\circ$ ), the estimated  $C_L$  at  $\alpha = 0$  is 0.0035. This corresponds to an error of 0.3% compared to the maximum  $C_L$ .

### 2.3. Test matrix

In the experiments, two different sheeting variations were tested. First, a test matrix with several systematic sheeting variations was conducted at different apparent wind angles. In each configuration, the middle sail (Sail 2) was fixed at a specific angle of attack, while the sheeting angles of the front sail (Sail 1) and the aft sail (Sail 3) were varied according to Table 2. The angles were chosen to capture both favorable sheeting trends and settings that was expected to affect the performance negatively. The angle of attack of the middle sail was first set at  $0^\circ$  followed by  $5^\circ$ ,  $10^\circ$ ,  $15^\circ$ ,  $17^\circ$  and  $19^\circ$ . The increment in angle of attack was reduced above  $15^\circ$  to increase the resolution near the point of sail stall.

Next, tests were conducted in which the angle of attack was swept from low to high to investigate how interaction effects influenced the point of stall. Sail 2 was swept from  $\alpha_2 = -15^\circ$  to  $\alpha_2 = 20^\circ$ , while the other two sails remained stationary. The angles of attack of Sails 1 and 3, seen in Table 3, were chosen based on the previous systematic sheeting variations to generate high aerodynamic loads and a strong interaction effect on Sail 2.

Finally, tests were also conducted for a single sail, where the forward sail and the aft sail were removed and the roof balance was set to an angle corresponding to  $\beta_{AW} = 0^\circ$ . The remaining sail was then swept from  $0^\circ$  to  $20^\circ$  in steps of  $1^\circ$ .

In the following analysis, each sheeting and apparent wind angle variation is denoted on the form  $B\beta_{AW}A\alpha_1\alpha_2\alpha_3$ . Leading zeroes are included where applicable, in for example the case B15A000510. In cases where  $\alpha_i < 0$  the leading zero is replaced by a minus sign, e.g. B15A-50005.

## 3. Lifting line method for interacting wing sails (ISILL)

The main principles of the method are summarized below. A detailed description of the ISILL method may be found in previous publications by the authors (Malmek, 2023; Malmek et al., 2024). Two subsections follow the summary, Section 3.1 describes how the 2D sectional lift and drag is established and Section 3.2 gives a description of the viscous boundary layer correction.

The ISILL method separates the problem of establishing the 3D aerodynamic forces of interacting sails into two parts. First, given an input wind profile, the downwash generated by the trailing vortices and corresponding loads on a specific sail are estimated by the SILL model (Persson and Werner, 2019). This step is followed by estimating the effect of sail–sail interaction by calculating the induced velocities created by all surrounding sails.

The single-sail SILL model can be summarized in the following main steps:

1. The geometry of the sail is discretized into spanwise strips (here 150). On each strip,  $2D c_l$  and  $c_d$  are retrieved from pre-tabulated data based on the local angle of attack and wind speed.
2. The sectional forces are integrated to calculate the total lift and drag coefficients  $C_L^{2D}$  and  $C_D^{2D}$ , without downwash.
3. The 3D effect of the trailing vortices are estimated by assuming an elliptical lift distribution over the sail. The total finite-span  $C_L$  is estimated by the formula

$$C_L = \frac{C_L^{2D}}{1 + \frac{2}{AR}}, \quad (2)$$

and the total drag coefficient,  $C_D$ , by

$$C_D = \frac{C_L^2}{\pi AR} + C_D^{2D}. \quad (3)$$

By using an assumed lift distribution, the calculation time is reduced and the stability of the code increased. There is the possibility of correcting Eq. (2) for planform deviations, as suggested, for example, by Schrenk (1940), but this type of correction has been deemed unnecessary in the present geometry.

Having estimated the total forces on each sail by the SILL model, the sail–sail interaction effects are modeled with a potential flow-based vortex model:

1. The total circulation strength is calculated by the Kutta-Jukovski theorem (using averaged local wind conditions) and distributed over the sail span, again assuming an elliptical distribution.
2. Each sail is represented by a system of horseshoe vortices with constant strength. The change in circulation strength between each spanwise strip determines the strength of the vortices.
3. At each control point, the Biot-Savart law allows calculating the induced velocities generated from all surrounding sails. These are summarized and added to the input wind profile, giving a new, sail-specific, local input wind profile.

In the current implementation, the following is applied: (1) the generated lift and drag forces are assumed to apply in the quarter-chord; (2) the induced velocities from surrounding sails are estimated at the three-quarter chord; and (3) the sails are mirrored in the tunnel roof and walls (not floor). The discretization scheme and placement of the control points are similar to the finite-step method by Weissinger. (Weissinger, 1947; Van Dam, 2002).

In this paper, the method is used and evaluated only under steady-state conditions, and a uniform profile of the far-field inflow is assumed.

### 3.1. Sectional lift and drag calibration using single-sail results

In the ISILL method, sectional  $2D c_l/c_d$ -data as a function of the effective angle of attack is required as input. These data can be estimated by, for example, 2D CFD simulations or wind tunnel experiments with an infinite aspect ratio. In this study, 2D CFD simulations were rejected because the flow was within the transitional regime and the wingsails were equipped with zigzag transition tape, making the CFD results very sensitive to different transition modeling strategies and assumed tunnel turbulence intensity levels. Experimental results for 2D / infinite wings, some presented in Fig. 2, were also evaluated as input. However, no 2D wind tunnel results were found for a NACA0015 section at the correct Reynolds number using zigzag transition tape at the quarter chord.

Instead, an alternative approach is suggested, where the 3D single-sail wind tunnel experiments, plotted in Fig. 3, are used to calibrate the sectional input data. This approach is motivated by two arguments; 1) it allows for evaluating the ability of the ISILL method to predict sail–sail interaction effects compared to not considering interaction (SILL);

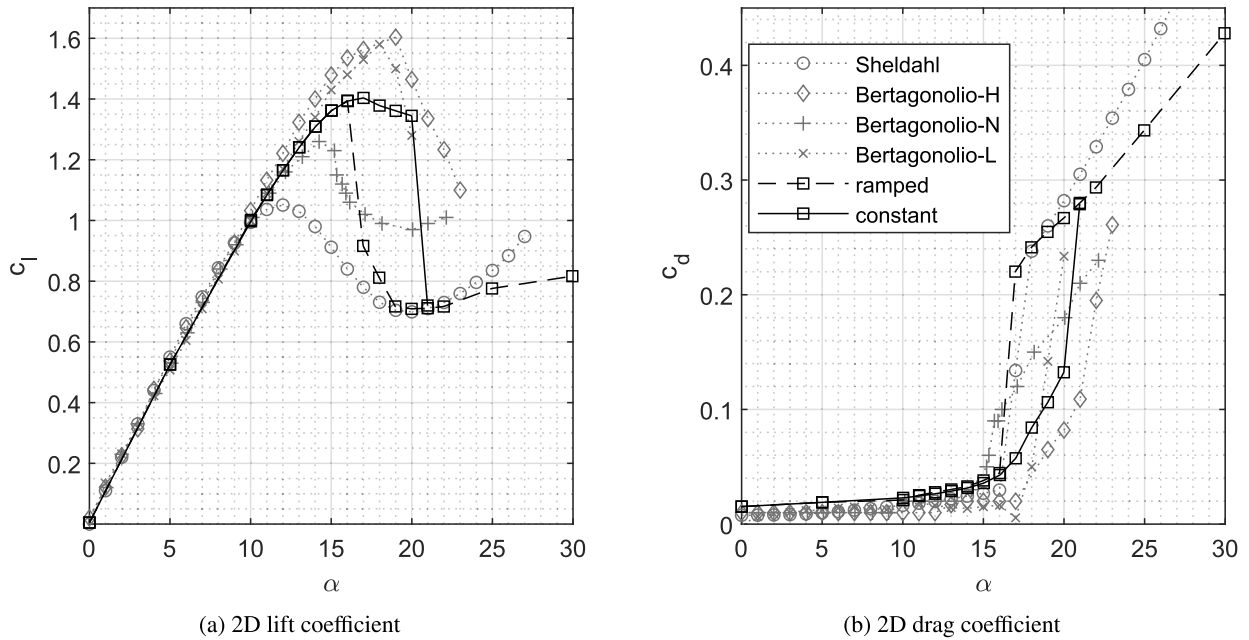


**Fig. 2.** 2D sectional  $c_l(\alpha)$  and  $c_d(\alpha)$ , used for model input. “Ramped” and “constant” refer to the two different calibrated input curves based on different wind tunnel test procedures. Wind tunnel data for the NACA0015 profile at two different Reynolds numbers,  $Re = 0.7 \times 10^6$  (Sheldahl and Klimas, 1981) and  $Re = 1.6 \times 10^6$  (Bertagnolio, 2008), are also presented. Bertagnolio (2008) reports results with three different turbulence levels — using a high-solidity turbulence grid (H), a low-solidity turbulence grid (L) and no turbulence grid (N).

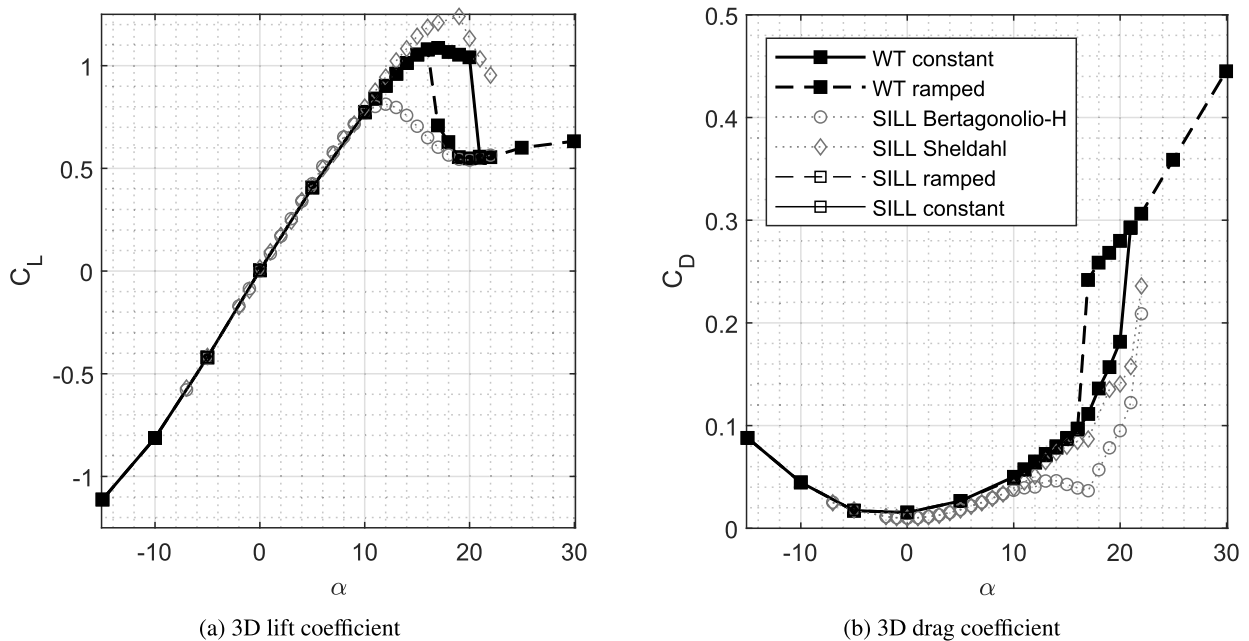


**Fig. 3.** 3D  $C_l(\alpha)$  and  $C_d(\alpha)$  for a single sail. Two different series of wind tunnel test (WT) results are presented, conducted at two different in-between tests of wind speeds. In the first series, the speed was maintained constant at 25 m/s, in the second series the speed was lowered to 10 m/s while changing the angle of attack. The results using the SILL model with two different sets of experimental input data (see Fig. 2) are also presented. Due to the calibration, the SILL model results using the 2D ramped and constant data tables coincide with the 3D wind tunnel tests.

and 2) this procedure is in line with industry application of the code in VPPs, as 3D single-sail CFD simulations or experimental results are often available.

The calibrated sectional  $c_l/c_d$ -data are plotted in Fig. 2, along with experimental reference data for the NACA0015 profile (Bertagnolio, 2008; Sheldahl and Klimas, 1981). It can be concluded that the maximum lift coefficient and stall angle are sensitive to Reynolds number effects as well as to turbulence levels in the wind tunnel.

Note that at higher angles of attack, there are two different data sets, based on the wind speed between the tests, as discussed in Section 2.2.

To ensure stability of the ISILL code under post-stall conditions, angles of attack higher than  $\alpha = 30$  are required in the input table. There are no single-sail data available from the RJ Michel wind tunnel tests, and in the absence of such data, the AERODAS model by Spera (2008) has been implemented to approximate the post-stall lift and drag curves.

### 3.2. Correcting for boundary layer interaction effects

A limitation of ISILL is that the input sectional data is obtained for a single sail. However, when multiple sails are introduced, the incoming flow to each sail is twisted by the sail–sail interaction. This disturbance from the surrounding sails is evaluated at a single control point on each sail strip using potential flow theory. Despite this simplification, the approximation has shown adequate results before the onset of stall (Phillips and Snyder, 2000).

Consequently, no consideration is given to the chord-wise pressure variation due to interaction. However, this affects the development of the boundary layer, particularly when the trailing edge of a sail is oriented close to the leading-edge low pressure of a following sail. This interaction-induced reduction of the pressure gradient over the boundary layer delays its separation. Consequently, under certain conditions, higher angles of attack can be sustained before the sail stalls, producing a higher maximum lift force.

In the ISILL model, this effect is accounted for by an empirical correction of the lift force. The correction postpones the angle of stall by adding an inviscid component to the viscous input sectional lift coefficient. The weight between the two is determined by an empirical expression based on the interaction-induced pressure change along the rear three-quarters of the section. A detailed description can be found in Malmek et al. (2024), and the same correction settings are applied here.

## 4. Results and discussion

This section presents and analyses the results from the validation of the aerodynamic interaction method ISILL against wind tunnel experiments. The systematic sheeting variations are presented in Section 4.2 and the sheeting sweeps in Section 4.3. ISILL is compared both to the experimental results and the single-sail SILL model, which does not consider sail–sail interaction. In all plots, the wind tunnel results are marked by black squares, the ISILL method by yellow knots and the SILL model by red crosses.

The method has been set to best reflect the conditions for the specific wind tunnel run. As input to the model, the effective angle of attack *measured* in the experiment has been used. This effective angle may differ by up to 0.5° from the angle of attack specified by the sheeting case. Note that in all figures, the specified angle of attack is used as legend. In addition, the effective average wind speed and air density are used in the calculations, which may vary slightly from test to test. The ISILL results have been corrected for side wall mirroring effects, discussed in Section 4.1, by including three imaginary sail triplets on each side of the real sails.

Two statistical measures are used in this section: the mean absolute error (MAE) and the mean signed deviation (MSD). They are defined by the following equations:

$$\text{MAE} = \frac{1}{n} \sum_{i=1}^n |\hat{y}_i - y_i| \quad \text{and} \quad (4)$$

$$\text{MSD} = \frac{1}{n} \sum_{i=1}^n (\hat{y}_i - y_i), \quad (5)$$

where  $n$  is the number of observations,  $\hat{y}_i$  is the predicted value and  $y_i$  is the observed value in the experiments.

### 4.1. Blockage effects and wall mirroring

In earlier studies, Wielgosz et al. (2025), Xu et al. (2025) CFD investigations in a single-sail setup concluded that there were no blockage effects that affected the results. However, in test cases with all three sails under high aerodynamic load, an effect of the tunnel walls was observed. In lifting line modeling, it is customary to identify flat surfaces as mirror boundaries, for example, when assuming the sail has a double

span when placed on a large flat deck. This assumption was extended to investigate potential mirroring effects in the tunnel side walls, by modeling them as reflective boundaries. The mirroring effect of the flow on the tunnel floor was assumed to be minimal due to the large distance from the sail tips to the tunnel floor and the smaller interaction effect from the trailing vortices compared to the vertical vortices.

For each different  $\beta_{AW}$ , the case with maximum sail load was selected: B15A101520, B30A101520, B60A131516 and B90A161514. The convergence of total  $C_X$  and  $C_L$  as a function of the number of mirrors was investigated and related to a maximum of 5 mirror images in each side wall. The convergence of total  $C_X$  and  $C_L$  as a function of the number of mirrors was investigated, considering up to 5 mirror images on each side wall. The largest difference in  $C_X$  was 8% when no wall mirrors were used, 0.55% with 2 mirrors on each side, and 0.12% with 3 mirrors on each side. The force coefficients were unaffected when increasing from 4 to 5 mirrors, with less than 0.00% difference.

### 4.2. Systematic sheeting variations

This section summarizes the results for the systematic sheeting variations described in Table 2. The investigated variables are the total predicted driving<sup>1</sup> force,  $C_X$ , and the yaw moment coefficient,  $C_M$ . These were chosen due to their strong influence on overall vessel performance in a VPP. Errors in  $C_X$  prediction lead to inaccurate speed expectations. Similarly, errors in yaw moment estimation result in under- or overestimating rudder angles, which can affect both vessel speed and maneuverability.

Figs. 4–7 present scatter plots of  $C_X$  and  $C_M$  at four different apparent wind angles from sailing close hauled to beam reach. Tables 4 and 6 present aggregated results for the prediction of the driving force coefficient. Tables 5 and 7 summarize the results of the prediction of the yaw moment.

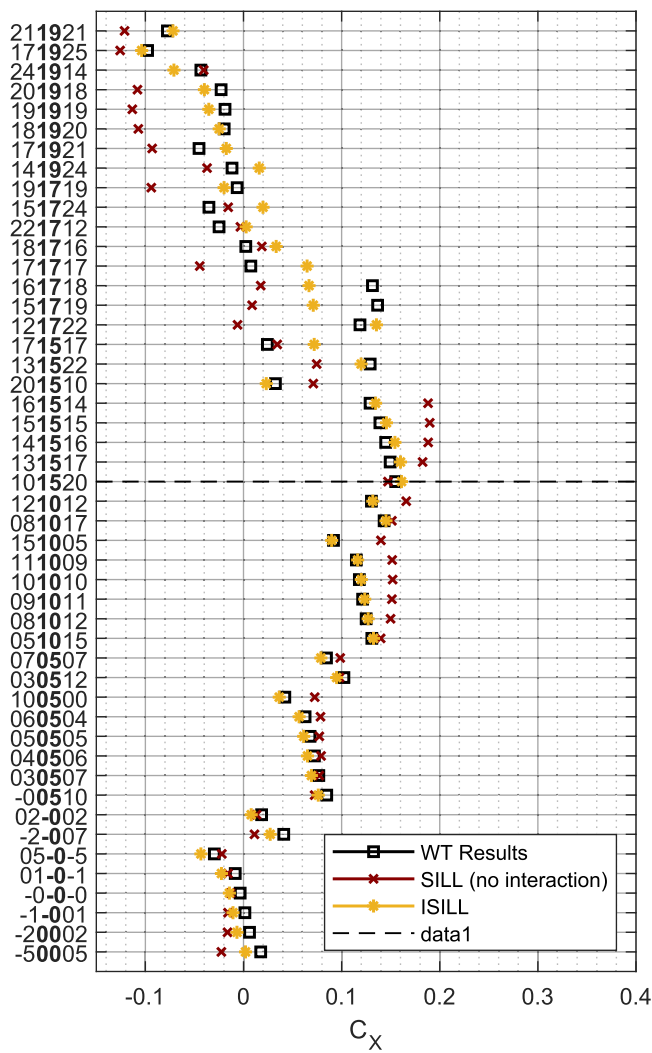
#### 4.2.1. Sailing very close hauled $\beta_{AW} = 15^\circ$

An apparent wind angle of 15° corresponds to when a ship is sailing very close to the wind. Consequently, the total driving force, shown in Fig. 4(a), is relatively low. This is because the direction of the generated lift force is nearly orthogonal to the direction of the driving force. At this low apparent wind angle, the negative effect of the drag force on the driving force becomes considerable. However, the positive lift force projected in the  $x$ -direction (forwards) is more than twice as large as the drag force projected in the aft direction, resulting in a positive  $C_X$ .

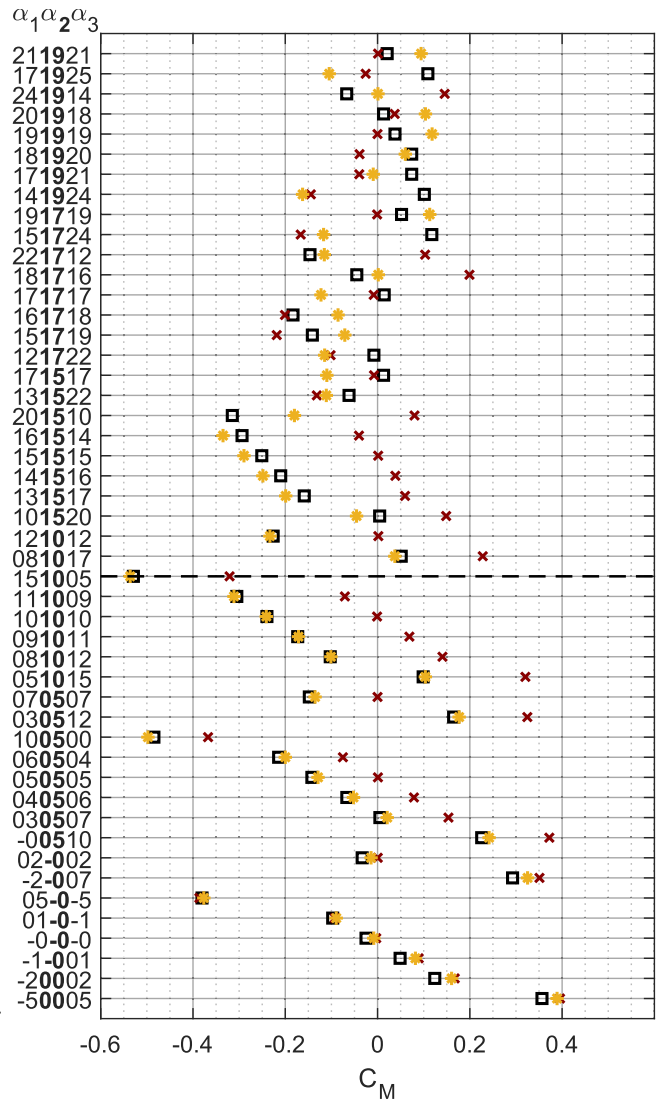
Up to the point of sail stall, the difference in  $C_X$  between ISILL and the experiments is small for this apparent wind angle, with a mean absolute error (MAE) of 0.007. The corresponding value for SILL is 0.019. In addition, ISILL correctly predicts the sheeting combination generating the maximum driving force coefficient ( $C_X^{\max}$ ), B15A101520. There is a positive trend of applying the interaction model even for the sheeting cases above the point of maximum driving force, despite the increased disagreement between the experiments and the model in certain instances.

The yaw moment coefficient,  $C_M$ , is shown in Fig. 4(b). Its minimum,  $C_M^{\min}$ , is observed for a different sheeting case, B15A-50005, compared to the case of  $C_X^{\max}$ . For lower sail loading, with  $\alpha_2$  fixed at 0°, the effects of sail–sail interaction are minimal. However, as the angles of attack increase, the sail–sail interaction significantly impacts the yaw moment. This is due to the increased load on the forward sail and the decreased load on the aftmost sail.

<sup>1</sup> Note that only the sails and no ship is present in the experiments; therefore, the driving force is defined in the longitudinal direction of an “imaginary” ship; since no drift is considered, this direction is assumed to coincide with the direction of motion.



(a) Total driving force coefficient.



(b) Yaw moment coefficient.

Fig. 4. Comparison of experimental and predicted driving force ( $C_X$ ) and yaw moment ( $C_M$ ) for  $\beta_{AW} = 15^\circ$ .

Table 4

Predicted maximum driving force coefficient and corresponding angles of attack, sailing close hauled. The model with (ISILL) and without (SILL) interaction effects considered is compared to the experimental results (WTT).

	$\beta_{AW} = 15^\circ$				$\beta_{AW} = 30^\circ$			
	$C_X^{max}$	$\alpha_1$	$\alpha_2$	$\alpha_3$	$C_X^{max}$	$\alpha_1$	$\alpha_2$	$\alpha_3$
WTT	0.155	10°	15°	20°	0.417	10°	15°	20°
ISILL	0.161	10°	15°	20°	0.436	13°	15°	17°
SILL	0.190	15°	15°	15°	0.452	15°	15°	15°
$e_{ISILL}$	3.8%	0°	0°	0°	4.7%	3°	0°	-3°
$e_{SILL}$	22.4%	5°	0°	-5°	8.6%	5°	0°	-5°

Table 5

Predicted minimum yaw moment coefficient and corresponding angles of attack, sailing close hauled. The model with (ISILL) and without (SILL) interaction effects considered is compared to the experimental results (WTT).

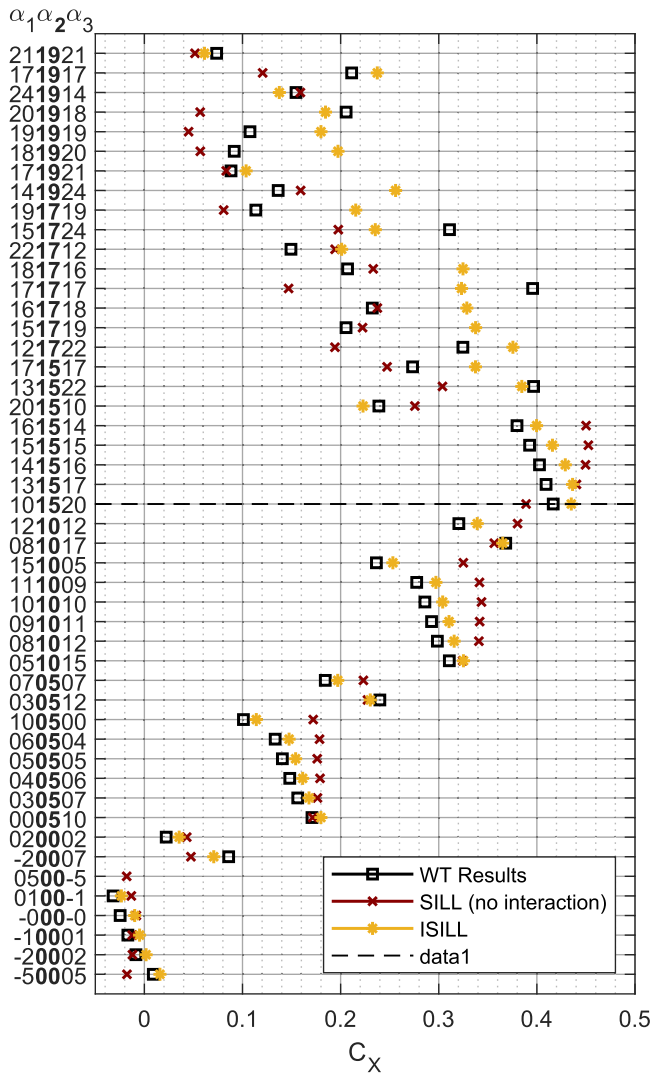
	$\beta_{AW} = 15^\circ$				$\beta_{AW} = 30^\circ$			
	$C_M^{min}$	$\alpha_1$	$\alpha_2$	$\alpha_3$	$C_M^{min}$	$\alpha_1$	$\alpha_2$	$\alpha_3$
WTT	-0.529	15°	10°	5°	-0.493	15°	10°	5°
ISILL	-0.536	15°	10°	5°	-0.458	15°	10°	5°
SILL	-0.386	5°	-0°	-5°	-0.346	5°	0°	-5°
$e_{ISILL}$	1.3%	0°	0°	0°	-7.1%	0°	0°	0°
$e_{SILL}$	-27.0%	-10°	-10°	-10°	-29.7%	-10°	-10°	-10°

4.2.2. Sailing close hauled,  $\beta_{AW} = 30^\circ$

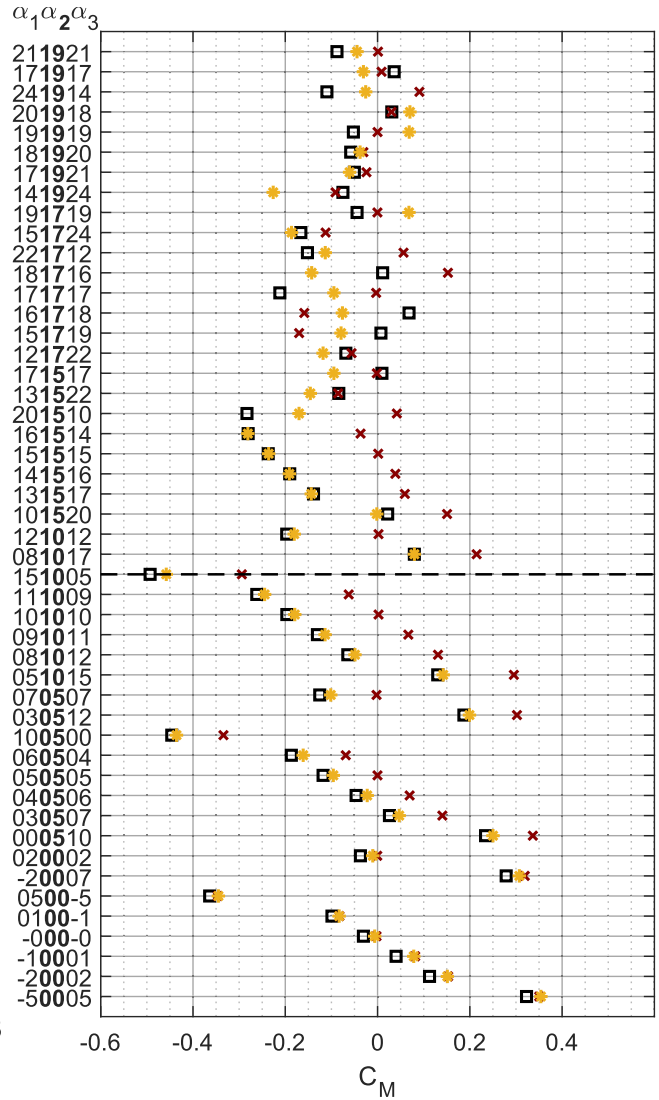
At an apparent wind angle of  $30^\circ$  (Fig. 5), the driving force is nearly doubled due to the more favorable wind angle compared to  $\beta_{AW} = 15^\circ$ . The ISILL method effectively captures the general trend of the interaction effect for different sheeting cases. In contrast, the SILL model, which does not consider interaction, predicts a higher driving force than the experiments in several cases. The most favorable sheeting configuration is found in the initial validation cases of each group, where the sheeting angle of Sail 1 is increased (i.e.  $\alpha_1$  decreased) by  $3^\circ$ - $5^\circ$  and the sheeting

angle of Sail 3 decreased by  $3^\circ$ - $5^\circ$  to compensate for the change in the local angle of attack. The ISILL method accurately predicts the decrease in driving force for cases B30A131520-B30A201510, although the case with the highest total driving force is predicted to be B30A131520 rather than B30A101520, as indicated by the experiments.

A case of special interest is B30A171717, where the ISILL method predicts that Sail 1 has begun to stall ( $C_L = 1.00$ ). The model underestimates the positive effect of the sail-sail interaction, as the lift force ( $C_L = 1.33$ ) is approximately 30% higher in the experiments. The rea-



(a) Total driving force coefficient.



(b) Yaw moment coefficient.

Fig. 5. Comparison of experimental and predicted driving force ( $C_X$ ) and yaw moment ( $C_M$ ) for  $\beta_{AW} = 30^\circ$ .

son behind the higher lift coefficient than the maximum  $C_L$  seen for the single sail in Fig. 3 is that the local flow velocity is increased.

Consistent with the results for  $\beta_{AW} = 15^\circ$ , the difference is small when comparing the yaw moment predicted by ISILL and the experiments. The agreement improves by considering the interaction effects, as can also be seen in Table 5.

For both close-hauled cases, it can be seen in Table 4 that the maximum driving force is reached at sheeting variation B15A101520 and B30A101520. This indicates that the sheeting variations were too conservative and that an even higher maximum driving force might be achieved by further adjusting the sheeting of Sail 1 and Sail 3.

The results show a bias deviation, where the driving force is slightly over-predicted with a mean absolute error of +0.013 for the cases up to  $C_X^{\max}$ . By studying the lift force coefficient for each sail it can be seen that the force on Sail 3 is systematically over predicted by ISILL with a mean signed deviation (MSD) of +0.052. The deviation occurs already at low angles of attack.

4.2.3. Sailing at a close reach,  $\beta_{AW} = 60^\circ$

As the sailing angle becomes more favorable, the generated driving force increases, and the interaction effects are less pronounced. Note the change in scale between Figs. 5(a) and 6(a). The prediction of the model

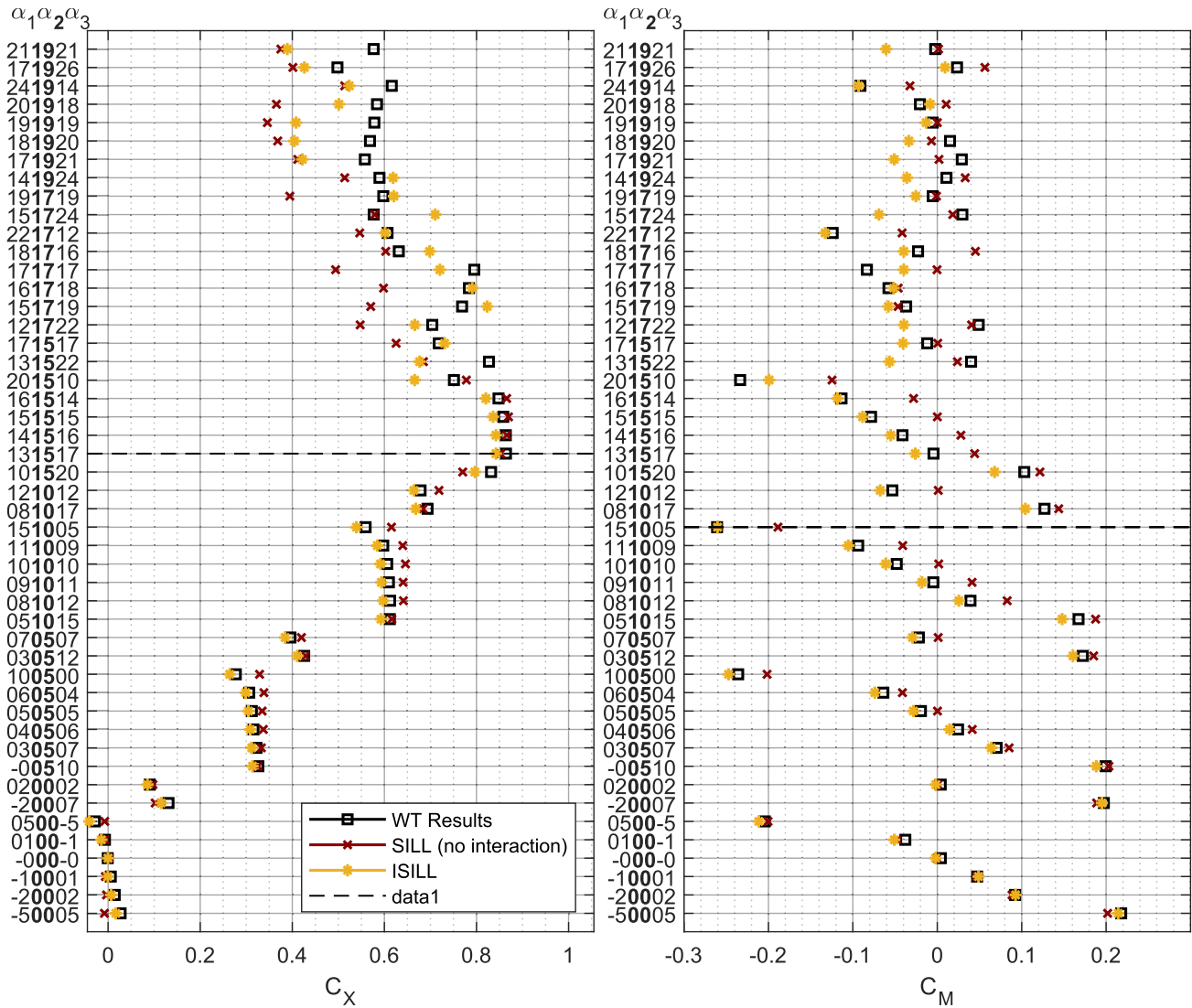
Table 6

Predicted maximum driving force coefficient and corresponding angles of attack, sailing close and beam reached. The model with (ISILL) and without (SILL) interaction effects considered is compared to the experimental results (WTT).

	$\beta_{AW} = 60^\circ$			$\beta_{AW} = 90^\circ$				
	$C_X^{\max}$	$\alpha_1$	$\alpha_2$	$\alpha_3$	$C_X^{\max}$	$\alpha_1$	$\alpha_2$	$\alpha_3$
WTT	0.864	13°	15°	17°	1.001	17°	15°	14°
ISILL	0.842	14°	15°	16°	1.005	17°	17°	17°
SILL	0.870	15°	15°	15°	1.054	15°	15°	15°
$e_{ISILL}$	-2.5 %	1°	-0°	-1°	0.5 %	0°	2°	3°
$e_{SILL}$	0.6 %	2°	-0°	-2°	5.4 %	-2°	0°	1°

is good up to the point of  $C_X^{\max}$  (B60131517) and the errors of ISILL and SILL (no interaction) are less than 2%, as presented in Table 6. In fact, the prediction of the maximum driving force is slightly better predicted by the SILL model, but not considering the interaction gives a large error in the yaw moment coefficient; see Table 7.

The general trend of decreasing driving force is predicted at higher angles of attack, but deviations increase drastically. This is also true for the prediction of the force distribution between the three sails, as indicated by the moment coefficients presented in Fig. 6(b).



(a) Total driving force coefficient. (b) Yaw moment coefficient.

Fig. 6. Comparison of experimental and predicted driving force ( $C_X$ ) and yaw moment ( $C_M$ ) for  $\beta_{AW} = 60^\circ$ .

Table 7

Predicted minimum yaw moment coefficient and corresponding angles of attack, sailing close and beam reached. The model with (ISILL) and without (SILL) interaction effects considered is compared to the experimental results (WTT).

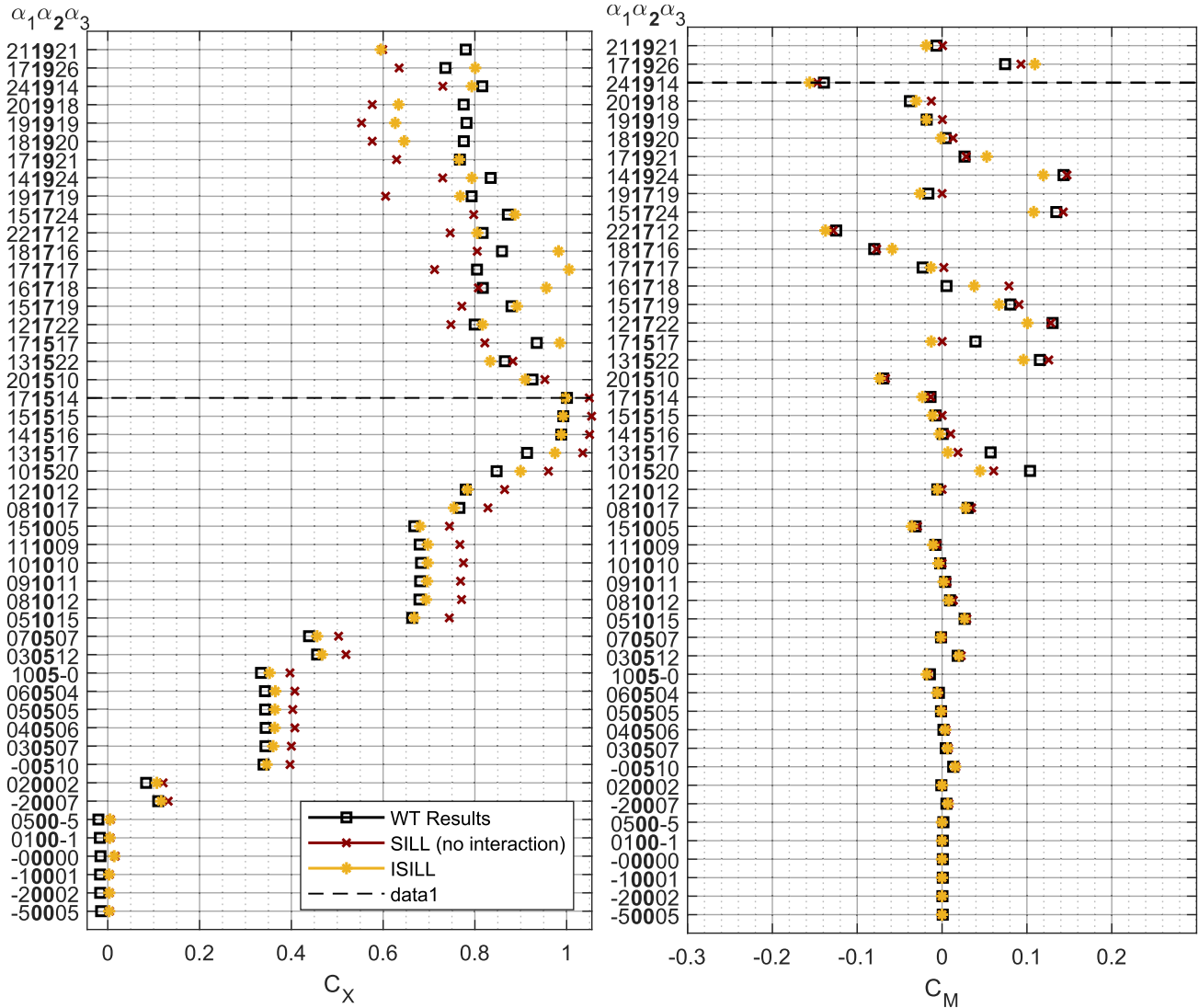
	$\beta_{AW} = 60^\circ$				$\beta_{AW} = 90^\circ$			
	$C_M^{\min}$	$\alpha_1$	$\alpha_2$	$\alpha_3$	$C_M^{\min}$	$\alpha_1$	$\alpha_2$	$\alpha_3$
WTT	-0.261	15°	10°	5°	-0.139	24°	19°	14°
ISILL	-0.260	15°	10°	5°	-0.156	24°	19°	14°
SILL	-0.202	10°	5°	0°	-0.147	24°	19°	14°
$e_{ISILL}$	-0.2%	0°	0°	0°	12.0%	0°	0°	0°
$e_{SILL}$	-22.7%	-5°	-5°	-5°	5.6%	0°	0°	0°

4.2.4. Sailing at beam reach,  $\beta_{AW} = 90^\circ$

The results of the sheeting configurations at  $\beta_{AW} = 90^\circ$  are presented in Fig. 7. Since the direction of the apparent wind is orthogonal to the x-axis, the driving force is equal to the total lift force  $C_L$ . There is no leeward component of the lift force that contributes to the side force,  $C_Y$ , in the transverse direction. Therefore, sailing at beam reach generates the highest driving forces and the smallest yaw moments of all validation cases.

However, there is an effect of the interaction that results in a decrease in driving force compared to the case where the three sails are unaffected by each other. The change in the local angle of attack is small, but it has an effect on the local wind speed. The foremost sail experiences an increase in wind speed, which has a positive effect on the generated lift. In contrast, the middle and aft sails experience a local decrease in wind speed, and the generated lift force is reduced compared to the case without interaction. ISILL predicts this behavior.

The absolute ISILL prediction of the maximum driving force corresponds well to the experiments, but the predicted optimal sheeting angles are incorrect. ISILL predicts the maximum driving force to occur for case B90A171717, with lift force coefficients from fore to aft 1.13, 1.01 and 0.89. The corresponding values in the experiments for the same case are 0.76, 0.80 and 0.86. The foremost and middle sails have stalled in the experiments, but not when modeled by ISILL. The explanation for this deviation could be due to the interaction being modeled using potential flow. However, when the ISILL prediction is compared with IDDES CFD results, a high-fidelity CFD model in which viscous effects are included, both models show a similar trend. Xu, Malmek and Bensow (2025) reports following lift coefficient values for Sail 1–Sail 3; 1.22, 1.06 and 1.01.



(a) Total driving force coefficient.

(b) Yaw moment coefficient.

Fig. 7. Comparison of experimental and predicted driving force ( $C_X$ ) and yaw moment ( $C_M$ ) for  $\beta_{AW} = 90^\circ$ .

Another possible explanation for the deviation for case B90A171717 is a hysteresis effect, which is not modeled in the simulations. In preceding runs, such as case B90A161718, Sail 1 and Sail 2 appear to have stalled in the experiments; in fact, Sail 2 stalled already for B90A121722. By studying the drop in lift force between  $\alpha = 16^\circ$  and  $\alpha = 17^\circ$  for the single-sail results in Fig. 3, it can be seen that there is a drastic change between these two angles (using ramped wind speed in-between test runs). As Sail 1 and Sail 2 have already stalled in the experimental runs preceding B90A171717, the positive effect of the interaction cannot generate a locally more beneficial angle of attack favorable enough to regain pre-stall characteristics.

The yaw moments plotted in Fig. 7(b) are small at low angles of attack. This is expected as the side force equals the drag force at  $\beta_{AW} = 90^\circ$ , which is very small compared to lift force at these low angles of attack. Additionally, the interaction between the sails is weaker, resulting in a more evenly distributed load over three sails. As the angle of attack increases, so does the drag force. This behavior is predicted by ISILL and SILL (no interaction), indicating that the drag is well predicted at higher angles of attack. As presented in Table 7, the percentage error in the minimum moment coefficient is higher for this apparent wind angle, but it can be observed that it occurs for a case well

above the point of stall and that the corresponding sheeting angles are correct.

#### 4.3. Stall study - sheeting sweep with the mid sail

This section presents results for sheeting sweep with Sail 2, the middle sail. Sweeps are presented at two apparent wind angles,  $\beta_{AW} = 30^\circ$  and  $\beta_{AW} = 90^\circ$ . The sheeting angles of the sails are set according to Table 3.

The sheeting sweep results at  $\beta_{AW} = 30^\circ$  are presented in Fig. 8, where the wind tunnel experiments are compared to the ISILL method and the SILL (no interaction). The lift and drag coefficients for each of the three sails are shown: Sail 2 with full lines, Sail 1 with dashed lines and Sail 3 with dotted lines. Although only Sail 2 changes angle, a clear interaction effect is seen on the forces generated by Sail 1 and Sail 3. For example, the lift force generated by Sail 3 is reduced by nearly 20%, compared to when not considering the interaction, when Sail 2 reaches  $\alpha_2 = 20^\circ$ . This behavior is captured by the ISILL method, yet a small error remains. The boundary layer correction (not shown in the figure) improves the predicted lift force on both Sail 1 and Sail 2 by ca 6%, however, additional tuning of the model could possibly im-

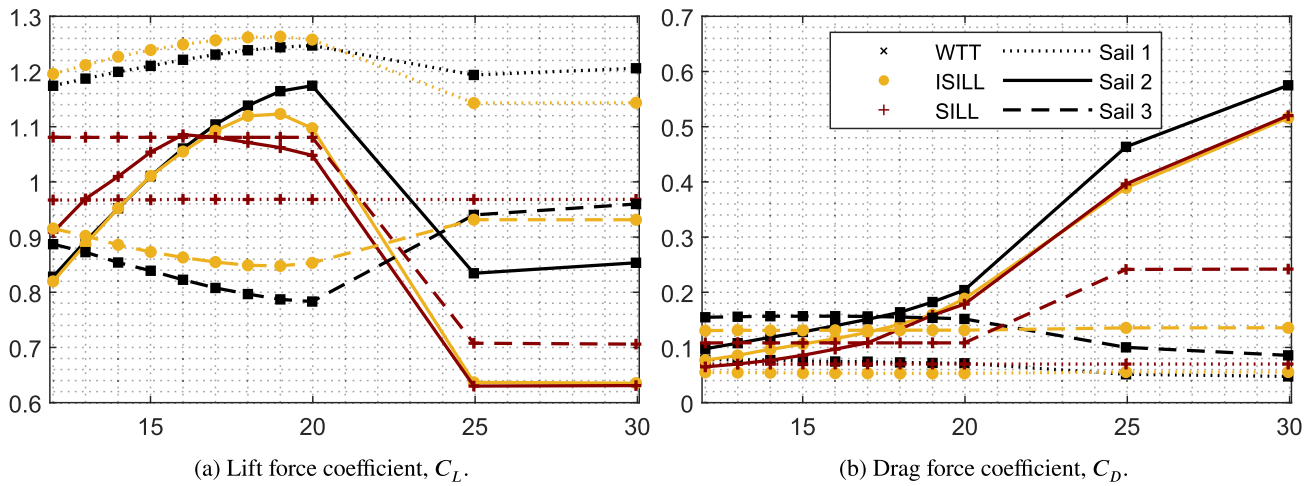


Fig. 8. Sail force coefficients when Sail 2 is swept from  $12^\circ$  to  $30^\circ$ , sailing at an upwind apparent wind angle of  $\beta_{AW} = 30^\circ$ . Sail 1 and Sail 3 are fixed. The ramped sectional input data was used for  $\alpha_2 \geq 25^\circ$ .

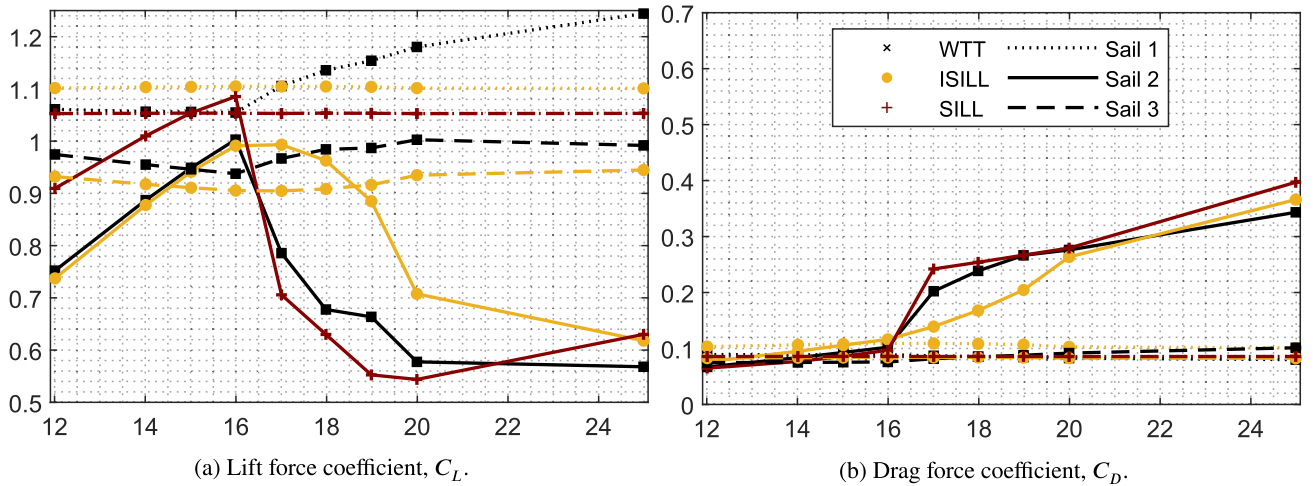


Fig. 9. Sail force coefficients when Sail 2 is swept from  $12^\circ$  to  $25^\circ$ , sailing at an apparent wind angle of  $\beta_{AW} = 90^\circ$ . Sail 1 and Sail 3 are fixed. The ramped sectional input data was used for all angles of attack.

prove the prediction of the maximum lift force and the onset of stall further.

In Fig. 8(a), it can be seen that even though Sail 3 is kept at a constant angle of attack, its generated lift force drops in the case without interaction (SILL) when Sail 2 goes from  $\alpha_2 = 20^\circ$  to  $\alpha_2 = 25^\circ$ . This is due to changing the input table in the model between the two angles, from the constant table to the ramped table. This change is done because the wind speed in the wind tunnel is lowered to 10 m/s between experimental run, see the discussion in Section 3.1.

The sweep results at  $\beta_{AW} = 90^\circ$  are presented in Fig. 9. For Sail 2, there is a ca 10% negative effect on the maximum lift coefficient due to the interaction, which is well captured by ISILL. ISILL does, however, somewhat overestimate the interaction effect on Sail 1 and Sail 3. As the lift force is overestimated for one sail and underestimated for the other, the prediction of the driving force is still good, as seen previously in Fig. 7(a).

Beyond the point of sail stall, ISILL, including interaction effects, fails to predict the drastic drop in lift force seen in the experiments for Sail 2. This drop is better predicted by not including the interaction model. Investigations show that this difference is not caused by the boundary layer correction, which, as expected, has no effect ( $< 0.1\%$ ) on the force predictions at  $\beta_{AW} = 90^\circ$ . Neither is this difference due to the presence of wall mirrors. A likely explanation to the different stall behavior is

that the angle of attack is constant over the entire sail span in SILL, whereas in ISILL there is a different, interaction dependent effective angle of attack at each section. Without interaction, the entire sail stalls when  $\alpha_2 \geq 17^\circ$ . Thus, using ISILL, the sail stalls gradually as each section reaches the stall criterion.

## 5. Conclusions

This paper studies a rapid model for predicting sail–sail interaction, at various sheeting angles and apparent wind angles, against wind tunnel experiments. The emphasis has been on investigating the predictions and stability of the method around the onset of stall. Key findings include:

- *Satisfactory prediction of stall onset.* The ISILL method showed good correspondence with wind tunnel measurements for pre-stall angles and at the point of stall.
- *Accuracy and method behavior post-stall.* The method predicts the general decrease in driving force after the point of stall, but in absolute values the errors increase drastically. There is no clear advantage of applying the interaction model in the post-stall regime, but both SILL and ISILL remain computationally stable.

- *Generation of sectional input data.* The input of the method is calibration using 3D standalone sail data. The validation results show that this is a suitable approach, especially for predicting stall behavior.

Accurate predictions of maximum forces are key in establishing system performance. To do so, the point of stall onset must be established. The ISILL method provides adequate predictions of the maximum driving force, the yaw moment, and the corresponding sheeting angles. The improvement compared to not considering interaction is especially large in upwind sailing conditions and most notably for the yaw moment. The results highlight that the sail–sail interaction needs to be considered in order to correctly establish the balance of a ship under sail. This affects the center of effort of the sails, requiring an increased rudder angle to counteract the sail forces.

The decreased accuracy of the model beyond the point of sail stall is expected of a lifting-line-based model, especially when considering the assumption of an elliptical lift distribution. The ISILL method should be used with care if applied in this regime. In practice, the sails should be ideally operated at pre-stall angles, both for optimal performance and safety. Therefore, the forces generated beyond the point of stall should have small implications in a standard VPP, predicting the sail performance route. However, the effect of stall may be present when simulating certain operating conditions, such as during a maneuver or when sailing in highly nonuniform inflow caused by, for example, wind gusts.

The approach of calibrating input data using 3D single-sail measurements aligns with the practical use in performance prediction calculations, where standalone 3D lift and drag data are commonly given by technology providers. Sources of these data can be 3D CFD simulations or wind tunnel testing. The standalone input data may include effects of, for example, a sail foot-gap. It is also possible to use data from 3D full-scale sea trials with single sails or rotors to calibrate the input data, as suggested by [Werner et al. \(2021\)](#).

An additional conclusion is that including the boundary-layer correction suggested by [Malmek et al. \(2024\)](#) improves the predicted lift force coefficient and the onset of stall. In this paper, the correction coefficients were based on 2D CFD simulations, performed at a different scale but for the same geometry. In cases where sheeting sweeps are available, the method may be further calibrated for the specific case.

The experimental results presented in this paper can serve as an important validation case for further studies within the field of wind propulsion. However, there are indications that some blockage/interaction effects due to the tunnel walls were present in the wind tunnel experiments. This effect was compensated for in the ISILL method by introducing mirrors in the tunnel walls, and this correction affected the driving force coefficient by up to 8%. This type of blockage effect should be considered in future experimental setups and model validations using the experimental data. It has been beyond the scope of this current paper to make further experimental data available, but the research group is actively undertaking initiatives to make them accessible.

Future studies should include how the performance of the method beyond stall can be improved, possibly by empirical corrections or disregarding the assumption of an elliptical lift distribution. Another important topic to consider is how to compensate for the hull–sail interaction. A current approach suggested in research ([Kolk, 2021](#); [Garenaux and Schot, 2021](#)) and currently tested in the industry, for example at RISE, is to superimpose bare-hull induced velocities on the input wind profile that is fed into the lifting line model. However, further validation studies of this approach are needed.

Overall, the ISILL method has proven to be a robust and computationally efficient tool for predicting sail–sail interactions, in pre-stall conditions and at the onset of stall. Unlike other proposed non-linear lifting line (NLL) codes in a wind propulsion context, ISILL applies an assumed lift distribution, which reduces calculation time and ensures code stability post-stall. In addition, the use of input data calibrated by standalone sail measurements and a boundary layer correction further

enhance the accuracy of the predictions. These features make the ISILL method a valuable tool in the design of wind propulsion systems and an enabler for further advances in sustainable shipping technologies.

### CRedit authorship contribution statement

**Karolina Malmek:** Writing - review & editing, Writing - original draft, Visualization, Validation, Methodology, Investigation, Formal analysis, Data curation, Conceptualization; **Lars Larsson:** Writing - review & editing, Supervision, Methodology; **Rickard E. Bensow:** Writing - review & editing, Supervision; **Christian Finnsgård:** Writing - review & editing, Supervision, Funding acquisition.

### Data availability

Additional data may be available on request.

### Declaration of Generative AI and AI-assisted technologies in the writing process

During the preparation of this work the author(s) used *Writefull for Overleaf* in order to improve readability and language. After using this tool/service, the author(s) reviewed and edited the content as needed and take(s) full responsibility for the content of the publication.

### Declaration of competing interest

The authors declare that they have no known competing financial interests or personal relationships that could have appeared to influence the work reported in this paper.

### Acknowledgment

This research was funded by The Swedish Energy Agency (grant number 2022/P2021-00275) and The Swedish Transport Agency (grant number TRV 2024/99179).

### References

- Alterskjær, S.A., Eggers, R., Gao, Y., Kim, Y., Kume, K., Trodden, D., Werner, S., Zhang, X., 2024. Recommended Procedures and Guidelines - Predicting the Power Saving of Wind Powered Ships. Technical Report. Specialist Committee on Wind Powered and Wind Assisted Ships of the 30th International Towing Tank Conference (ITTC).
- Anderson, J.D., 1991. Fundamentals of Aerodynamics. McGraw-Hill. 2nd ed. <http://www.worldcat.org/isbn/9780073398105>.
- Babart, A., 2024. CN-AeroModels : A C++ implementation of aerodynamic models for wind propulsion systems of cargo ships. J. Open Source Softw. 9, 9–10. <https://doi.org/10.21105/joss.06940>
- Bertagnolio, F., 2008. NACA0015 measurements in LM wind tunnel and turbulence generated noise. Technical Report November. Risø Nationallaboratoriet for Bæredygtig Energi. Denmark. Forskningscenter Risøe. <http://forskningsbasen.deff.dk/Share.external?sp=S838d637b-17ce-48b6-80d0-d8e3562d42b9sp=Sdtu>.
- Beyer, Y., Ullah, J., Steen, M., Hecker, P., 2024. Unsteady nonlinear lifting line model for active gust load alleviation of airplanes. CEAS Aeronaut. J. 15 (4), 917–932. <https://doi.org/10.1007/s13272-024-00760-8>
- Castro, I.P., 2021. Calibration Tests in the Working Section of the R J Mitchell Wind Tunnel. Technical Report. University of Southampton.
- Dhomé, U., 2024. Experimental studies of wind and aerodynamics for wind-powered commercial ships. Ph.D. thesis. KTH royal institute of technology. <https://www.diva-portal.org/smash/record.jsf?pid=diva2\protect\protect\leavevmode@ifvmode\kern+.1667em\relax%3A1895789dswid=-6096>.
- Duport, C., Leroux, J.B., Roncin, K., Jochum, C., Parlier, Y., 2019. Benchmarking of a 3D non-linear lifting line method against 3D RANSE simulations. Houille Blanche 2019-Decem (5-6). <https://doi.org/10.1051/lhb/2019029>
- Gallay, S., Laurendeau, E., 2015. Nonlinear generalized lifting-line coupling algorithms for pre/poststall flows. AIAA J. 53 (7), 1784–1792. <https://doi.org/10.2514/1.J053530>
- Garenaux, M., Schot, J.J.A., 2021. Flettner Rotors performance and interaction effects on the marin hybrid transition coaster. In: RINA International Conference on Wind Propulsion. London, pp. 111–122. <https://doi.org/10.3940/rina.win.2021.13>
- Gerhardt, F.C., Werner, S., Li, D.-q., Malmek, K., 2022. Levelling the playing field : a numerical platform for the fair comparison of wind propulsion systems. In: International Conference on High Performance Marine Vehicles. Cortona, Italy, 29-31 August 2022, pp. 161–173.

- Giovannetti, L.M., Dhomé, U., Malmek, K., Persson, A., Wielgosz, C., 2022. Multi-wing sails interaction effects. In: The 24th Chesapeake Sailing Yacht Symposium. SNAME, Annapolis, Maryland, 10-11 June 2022, pp. 89–101.
- Graf, K., Hoeve, A.V., Watin, S., 2014. Comparison of full 3D-RANS simulations with 2D-RANS/lifting line method calculations for the flow analysis of rigid wings for high performance multihulls. *Ocean Eng.* 90, 49–61. <https://doi.org/10.1016/j.oceaneng.2014.06.044>
- IMO, 2023. 2023 IMO strategy on reduction of GHG emission from ships. *Int. Marit. Organ.* 4 (1), 18. <https://www.imo.org/en/MediaCentre/PressBriefings/pages/Revised-GHG-reduction-strategy-for-global-shipping-adopted-.aspx>
- Kolk, N. V.D., 2021. Aero-hydrodynamic interactions for wind powered ships : retrofit of a high-speed mega RoRo vessel. In: RINA International Conference on Wind Propulsion 2021. The Royal Institution of Naval Architects, pp. 241–256.
- Kolodziejski, M., Sosnowski, M., 2025. Review of wind-assisted propulsion systems in maritime transport. *Energies* 18 (4). <https://doi.org/10.3390/en18040897>
- Kramer, J., Steen, S., 2022. Sail-induced resistance on a wind-powered cargo ship. *Ocean Eng.* 261 (February), 111688. <https://doi.org/10.1016/j.oceaneng.2022.111688>
- Malmek, K., 2023. Rapid aerodynamic method for interacting sails. [https://research.chalmers.se/publication/534908/file/534908\\_Fulltext.pdf](https://research.chalmers.se/publication/534908/file/534908_Fulltext.pdf).
- Malmek, K., Dhomé, U., Larsson, L., Werner, S., Ringsberg, J., Finnsgård, C., 2020. Comparison of two rapid numerical methods for predicting the performance of multiple rigid wing-sails. In: *Innovsail. Innovsail 2020*, p. 10.
- Malmek, K., Larsson, L., Werner, S., Ringsberg, J.W., Bensow, R., Finnsgård, C., 2024. Rapid aerodynamic method for predicting the performance of interacting wing sails. *Ocean Eng.* 293. <https://doi.org/10.1016/j.oceaneng.2023.116596>
- OceanWings, 2024. Canopée RoRo, equipped with four lowerable fixed wingsails (OW LF). <https://www.oceanwings.com/use-case/ro-ro-canopee>.
- Parliament, E., 2023. Regulation (EU) 2023/1805 of the European parliament and of the council on the use of renewable and low-carbon fuels in maritime transport, and amending directive 2009/16/EC. *Office J. Eur. Union* 66 (July), 48–100. <https://doi.org/10.2771/793264.22.9.2023>
- Persson, A., Werner, S., 2019. Performance prediction of wind propulsion systems isig 3D CFD and route simulation. In: RINA International Conference on Wind Propulsion 2019. The Royal Institution of Naval Architects, London, pp. 20–30.
- Phillips, W.F., Snyder, D.O., 2000. Modern adaptation of Prandtl's classic lifting-line theory. *J. Aircr.* 37 (4), 662–670. <https://doi.org/10.2514/2.2649>
- Schot, J. J.A., Garenaux, M., 2023. Modelling of aerodynamic interaction effects for wind propulsion applied in commercial shipping: development of a non-linear lifting line method. In: *Proceedings of the 6th International Conference on Innovation in High Performance Sailing Yachts and Wind-Assisted Ships*, p. 381-412.
- Schrenk, O., 1940. A simple approximation method for obtaining the spanwise lift distribution. Technical Report. NASA Technical Reports Server. <https://ntrs.nasa.gov/citations/19930094469>.
- Sheldahl, R.E., Klimas, P.C., 1981. Aerodynamic Characteristics of Seven Symmetrical Airfoil Sections Through 180-Degree Angle of Attack for Use in Aerodynamic Analysis of Vertical Axis Wind Turbines. Sandia National Laboratories .
- Spera, D.A., 2008. Models of lift and drag coefficients of stalled and unstalled airfoils in wind turbines and wind tunnels. Technical Report. NASA Technical Reports Server. <https://ntrs.nasa.gov/citations/20090001311>.
- Van Dam, C.P., 2002. The aerodynamic design of multi-element high-lift systems for transport airplanes. *Prog. Aerosp. Sci.* 38 (2), 101–144. [https://doi.org/10.1016/S0376-0421\(02\)00002-7](https://doi.org/10.1016/S0376-0421(02)00002-7)
- Veritas, B., 2024. Wind Propulsion Technology Report. Technical Report. Marine & Off-shore Global Marketing and Communications. <https://marine-offshore.bureauveritas.com/newsroom/wind-propulsion-report>.
- Weissinger, J., 1947. The lift distribution of swept-back wings. Technical Report. NACA TM 1120. NASA Technical Reports Server. <https://ntrs.nasa.gov/citations/20030064148>.
- Werner, S., Nisbet, J., Hörteborn, A., Nielsen, R., 2021. Speed trial verification for a wind assisted ship. In: RINA International Conference on Wind Propulsion 2021. The Royal Institution of Naval Architects, pp. 62–72.
- Werner, S., Papanikolaou, A., Razola, M., Fagergren, C., Dessen, L., Kutenkeuler, J., Santén, V., Steinbach, C., 2023. The Orcele Project - Towards Wind-Powered Ships for Deep Sea Cargo Transport. SNAME Maritime Convention, SMC 2023 , 27–29. <https://doi.org/10.5957/SMC-2023-089>
- Wielgosz, C., Blackert, E., Giovannetti, L.M., Wallin, S., Kutenkeuler, J., Werner, S., 2025. The importance of scale effects for wind propulsion : experimental and numerical analysis of a wing sail. In: *The 25th Chesapeake Sailing Yacht Symposium. Annapolis, Maryland*, pp. 1–18.
- Xu, K., Malmek, K., Bensow, R., 2025. Numerical investigation of multiple wingsails interaction under different apparent wind angles. *Ocean Eng.* 336 (May), 121712. <https://doi.org/10.1016/j.oceaneng.2025.121712>
- Zhu, H., Yao, H.D., Ringsberg, J.W., 2024. Unsteady RANS and IDDES studies on a telescopic crescent-shaped wingsail. *Ships Offshore Struct.* 19 (1), 134–147. <https://doi.org/10.1080/17445302.2023.2256601>